

Article

Electrospinning of ZIF-67 Derived Co-C-N Composite Efficiently Activating Peroxymonosulfate to Degrade Dimethyl Phthalate

Guowei Pang, Min Ji, Zhuoran Li, Zhengwu Yang, Xiaojie Qiu and Yingxin Zhao *

School of Environmental Science & Engineering, Tianjin University, Tianjin 300350, China; pgwdahaoren@163.com (G.P.); jimin@tju.edu.cn (M.J.); lizhuoran7201@163.com (Z.L.); yzw_w1@163.com (Z.Y.); qiuxiaojie6097@163.com (X.Q.)

* Correspondence: yingxinzhao@tju.edu.cn

Abstract: In this work, an efficient cage-core peroxydisulfate (PMS) catalyst was synthesized by applying an electrospinning–calcination process to the cobalt–zeolitic imidazole framework (ZIF-67) crystals for the catalytic degradation of dimethyl phthalate (DMP). The morphology and surface properties of the synthesized materials (ZIF-67, Z600 and ZP400/600/800) were well characterized. ZP600 showed great performance for the catalytic degradation of DMP in the initial pH range of 7.5–10.5. The removal rate of DMP could reach 90.4% in 60 min under optimum dosages of reagents (catalyst = 0.1 g/L, PMS = 0.5 mM, DMP = 6 ppm), and the mineralization degree of contaminant could reach 65%. By quenching experiments, it was determined that sulfate radical ($\text{SO}_4^{\cdot-}$) and hydroxyl radical ($\cdot\text{OH}$) dominated the degradation process. Moreover, due to the good magnetism, ZP600 could be easily separated from liquid and showed great reusability in five-cycle reaction experiments. Surprisingly, with the cover of cage-like polyacrylonitrile (PAN) fibers, the cobalt leaching amount of ZP600 decreased by about 87%. This study would expand the application of the electrospinning process in the development of functional materials for water purification.

Keywords: electrospinning; ZIF-67; peroxydisulfate; cobalt leaching control

Citation: Pang, G.; Ji, M.; Li, Z.; Yang, Z.; Qiu, X.; Zhao, Y. Electrospinning of ZIF-67 Derived Co-C-N Composite Efficiently Activating Peroxymonosulfate to Degrade Dimethyl Phthalate. *Water* **2022**, *14*, 2248. <https://doi.org/10.3390/w14142248>

Academic Editor: Andrea G. Capodaglio

Received: 13 June 2022

Accepted: 14 July 2022

Published: 17 July 2022

Publisher's Note: MDPI stays neutral with regard to jurisdictional claims in published maps and institutional affiliations.



Copyright: © 2022 by the authors. Licensee MDPI, Basel, Switzerland. This article is an open access article distributed under the terms and conditions of the Creative Commons Attribution (CC BY) license (<https://creativecommons.org/licenses/by/4.0/>).

1. Introduction

Recently, with the continuous development of modern industry, the treatment of refractory wastewater has become an increasingly concerning problem [1]. Dimethyl phthalate (DMP) is one of the most common plasticizers for industry use [2]. It is also a typical pollutant in refractory wastewater, which is toxic to algae, invertebrates and fish and may also affect the human endocrine system [3]. Typical biological treatment systems are greatly affected by refractory wastewater, while other processes, such as adsorption, require further treatment of the used adsorbent [4]. As is known to us, advanced oxidation processes (AOPs) are effective means of degrading refractory pollutants [5]. Traditionally, AOPs include Fenton oxidation with hydroxyl radical ($\cdot\text{OH}$) as the main reactive oxygen species (ROS) and the sulfate radical-based advanced oxidation processes (SR-AOPs) with sulfate radical ($\text{SO}_4^{\cdot-}$) as the main functional component [6]. With the advantages of wider pH applicability, no sludge generation, a longer radical half-life and better reagent stability, SR-AOPs have drawn great attention in recent years [7–9].

It has been widely reported that transition metals ions, oxides and carbon materials are effective in activating peroxydisulfate (PMS) to generate ROS for water purification [10,11]. Among these, cobalt-based heterogeneous materials (cobalt oxides and composites) are considered to be some of the most effective activators because of their high performance, lower toxicity and reusable potential [12–14]. Anipsitakis et al. used commercial Co_3O_4 to activate PMS to degrade 2,4-dichlorophenol (2,4-DCP), and 85.2% of

DCP could be removed in 30 min [15]. Chen et al. successfully synthesized nano- Co_3O_4 with a small average particle size (20 nm), high specific surface area (18 m^2/g) and high catalytic degradation efficiency (100% of acid orange 7 was removed within 30 min) [16]. Recently, metal organic frameworks (MOFs), especially cobalt-containing MOFs, have been well developed as activators of PMS because of their regular particle size and high specific surface area, including pristine MOFs, MOFs-derived metal oxides and composites [17–19]. Studies have shown that the doping of carbon and nitrogen in metal catalysts helps to improve the dispersity of metal species and accelerate electron transfer, thus further improving the reaction efficiency [20,21]. Fortunately, polyacrylonitrile (PAN, $(\text{C}_3\text{H}_3\text{N})_n$), with rich carbon and nitrogen, can be used as a substance for electrospinning to develop catalysts by converting spinning precursors (polymer liquid mixture) into one-dimensional nanofibers using the electric field force [22]. It was reported that one-dimensional ZIF-67&PAN fibers (ZIF for zeolitic imidazole framework) were successfully synthesized by the electrospinning process for PMS activation [23]. With cubic ZIF-67 crystals uniformly immobilized on PAN fibers, the catalyst was easy to separate and reuse and showed good contaminants (acid yellow 17, tetracycline and bisphenol A) degradation performance under acidic conditions. Although the separation of catalysts was no longer a problem in that work, the stability and cobalt leaching of pristine MOF (ZIF-67) were not considered. It was reported that ZIFs were quite unstable under acidic conditions [24]. Moreover, metals in pristine MOFs were not as stable as the metals in calcined carbon materials, thus facing a greater risk of cobalt leaching in application. It was demonstrated that the cobalt leaching of $\text{Co}_3(\text{BTC})_2$ (a pristine MOF, BTC for benzene-1,3,5-tricarboxylic acid) could reach 105.2 mg/L, while its calcined derivative only leached 0.5 mg/L [25]. Inspired by the above, we believe that it is feasible to develop efficient and stable MOF-based carbon materials by applying an electrospinning–calcination process and simultaneously control the leaching of cobalt from MOF. The novelty of this work was that electrospinning as a novel technique was combined with calcination to improve the catalytic activity of ZIF-67 and control the cobalt leaching from it. Catalytic properties of catalysts synthesized at different calcination temperatures were evaluated. Moreover, multiple characterization methods were applied to analyze the probable mechanism of cobalt leaching reduction.

In this work, electrospinning was adopted as a method to enrich the content of carbon and nitrogen in a ZIF-67 (a cobalt-containing MOF) derived catalyst, and PAN was selected as the substrate of electrospinning. The aims of this study were to (1) develop novel cobalt-contained PMS activators by the electrospinning–calcination process and characterize the morphology and surface properties of the synthesized products; (2) evaluate the performance of ZP600 in PMS activation and investigate factors affecting the degradation process, including PMS dosage, initial pH, catalyst dosage and concentration of contaminant; (3) propose a probable activation mechanism of ZP600 and determine the dominated ROS in the system by quenching experiments; and (4) evaluate the reusability and cobalt leaching of the synthesized catalyst.

2. Materials and Methods

2.1. Chemicals

$\text{Co}(\text{NO}_3)_2 \cdot 6\text{H}_2\text{O}$, 2-methylimidazole (2-MeIM), potassium peroxymonosulfate ($2\text{KHSO}_5 \cdot \text{KHSO}_4 \cdot \text{K}_2\text{SO}_4$), N,N-dimethylformamide (DMF) and polyacrylonitrile (PAN, MW = 150,000) were purchased from Shanghai Macklin Biochemical Co., Ltd. (Shanghai, China). Anhydrous methanol (MeOH), anhydrous ethanol (EtOH), sodium hydroxide (NaOH), nitric acid (HNO_3), hydrochloric acid (HCl), acetonitrile, tert-butyl alcohol (TBA), furfuryl alcohol (FFA) and dimethyl phthalate (DMP, >99%) were obtained from Aladdin Chemical Co., Ltd. (Shanghai, China). Ultrapure water (18.2 $\text{M}\Omega \cdot \text{cm}$) was used in all experiments. All the reagents were used directly without further purification.

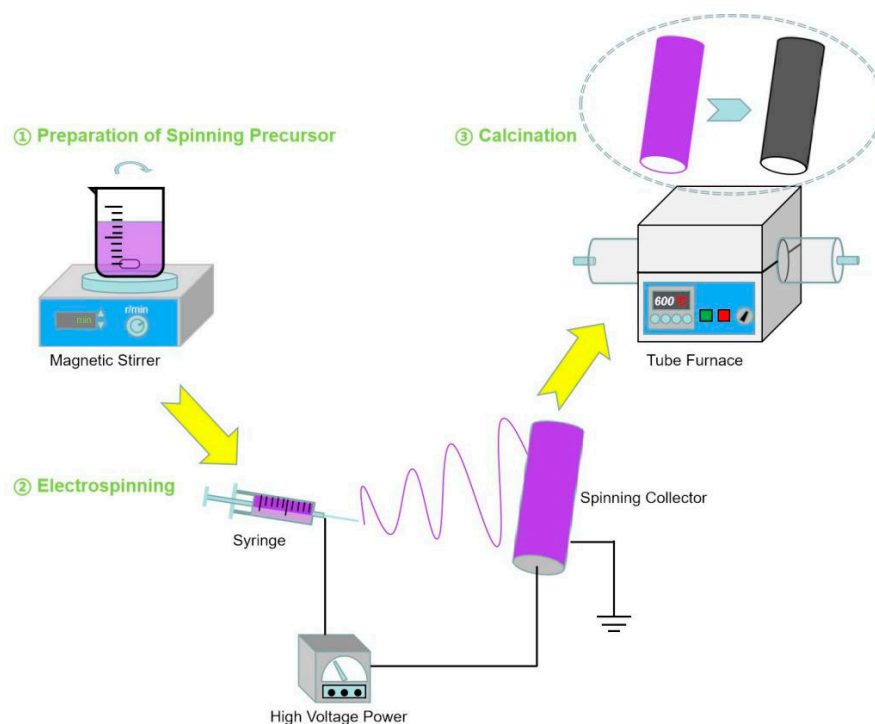
2.2. Sample Preparation

2.2.1. Preparation of ZIF67

ZIF-67 was synthesized by an improved hydrothermal method [26]. Typically, 0.225 g $\text{Co}(\text{NO}_3)_2 \cdot 6\text{H}_2\text{O}$ was dissolved in 6 mL of ultrapure water. Then, 2.75 g 2-MeIM in 40 mL of water was added to the above solution with stirring for 15 min at 60 °C. The mixture was kept at 60 °C for 20 h. The products were collected by centrifugation (5000 rpm, 5 min) and washed three times with ultrapure water and anhydrous methanol, respectively. The resulting sample was dried at 60 °C.

2.2.2. Preparation of ZP400/600/800 and Z600

In total, 0.8 g PAN was dissolved in 5 mL of DMF with stirring for 4 h. Then, 0.6 g ZIF-67 was added to the solution with stirring for another 4 h to obtain the uniform electrospinning precursor. The precursor was filled in a 5 mL syringe for the electrospinning process, which was carried out by applying a high positive voltage (15 kV). The distance between the needle tip and collector was 15 cm, and the injection speed was 0.1 mm/min. Aluminum foil was used to collect the electrospinning membrane. Finally, the collected membrane was heated to 400/600/800 °C for 2 h in an N_2 atmosphere with a ramp rate of 5 °C/min and then was cooled down to room temperature naturally. The resulting products were named ZP400/600/800 and ground into a powder for subsequent use. In addition, Z600 was synthesized by applying the same heating procedure to ZIF-67 powder. The schematic diagram of material synthesis was shown in Scheme 1.



Scheme 1. Illustration of the preparation process of ZP400, ZP600 and ZP800.

2.3. Characterization

The fabricated materials were characterized by several methods. Field emission scanning electron microscopy (FESEM) images were obtained on a Hitachi SU8020. Transmission electron microscopy (TEM) images were gained on a FEI Tecnai G2 F30. X-ray diffraction (XRD) patterns were analyzed by a D8 ADVANCE diffractometer (Bruker, Billerica, MA, USA). X-ray photoelectron spectrometry (XPS) spectra were analyzed by an escalab 250Xi (Thermo, Waltham, MA, USA). The magnetic property was measured on a Lake Shore 7404 vibrating sample magnetometer (VSM, Lake Shore, Columbus, OH, USA).

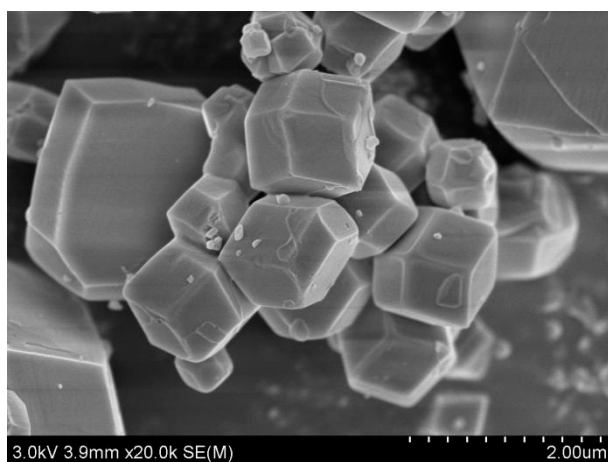
2.4. Catalytic Degradation of DMP

The degradation experiments were carried out in 250 mL beakers with 100 mL DMP solution at room temperature (controlled by an air condition system at 25 ± 2 °C). HNO_3 (0.1 mM) and NaOH (0.1 mM) were used to adjust the initial pH of DMP solution. Firstly, certain amounts of catalysts were added to the above solution for 30 min to achieve the adsorption/desorption equilibrium between the contaminant and catalyst. Then, PMS at a set amount was added to initiate the reaction. Magnetic stirring at a rate of 400 rpm was applied in the whole process of experiments. Samples (1 mL) were taken at set time intervals and quenched with 0.5 mL of methanol immediately. After filtering with 0.22 μm filters, samples were measured by an ultra-high-performance liquid chromatograph (UHPLC, Waters) equipped with a UV-Vis detector (Waters, detection wavelength: 224 nm) and a C18 column (Waters, 5 μm , 4.6 mm \times 250 mm) to determine DMP concentration with the mobile phase consisting of acetonitrile/water (*v/v*, 60/40) at a flow rate of 0.2 mL/min. Samples were taken at set time intervals and filtered with 0.45 μm filters for the determination of cobalt leaching and total organic carbon (TOC). The concentrations of cobalt ion leaching were analyzed by an iCAP7000 series inductively coupled plasma optical emission spectrometer (ICP-OES, Thermo, Waltham, MA, USA). The detection wavelength of ICP-OES was 228.6 nm and the working gas was argon. TOC values of samples were measured by a TOC analyzer (SHIMADZU, TOC-L). All experiments were performed at least two times to eliminate errors, and average results with standard deviation (error bars) were displayed in this work.

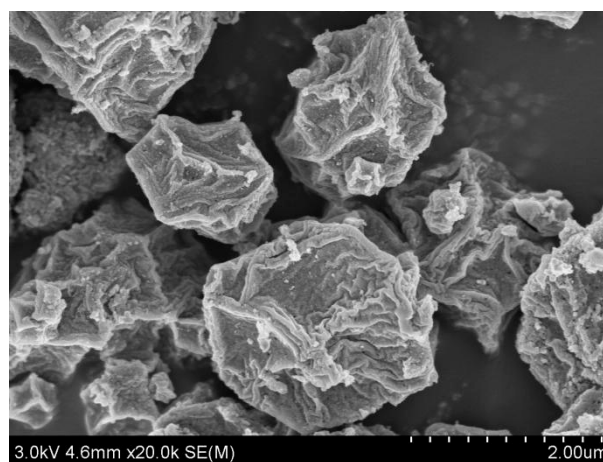
3. Results and Discussion

3.1. Characterization

SEM was applied to characterize the morphology of synthesized materials in this work. The uniform dodecahedral crystals shown in SEM image (Figure 1a) indicated the successful synthesis of ZIF-67. After calcination at 600 °C, the surface of ZIF-67 was wrinkled, as shown in the SEM image of Z600 (Figure 1b). The SEM image (Figure 1c) of ZP400 displayed a rough surface of the electrospinning–calcination material. While in ZP800 (Figure 1d), the coverage of ZIF-67 by PAN fiber was limited, and there was a risk of cobalt exposure. SEM images (Figure 1e,f) of ZP600 exhibited that PAN fibers covered carbonized ZIF-67 entirely and uniformly like a cage after electrospinning–carbonization processes. Wang et al. and Guo et al. both successfully synthesized ZIF-67&PAN fibers by electrospinning process, however, their product showed that many ZIF-67 cubes were fixed on a single PAN fiber, which was different from this study [23,27]. It can be speculated that the cage-like structure in ZP600 may have the effect of hindering cobalt leaching, which would be confirmed in the subsequent experiments.



(a)



(b)

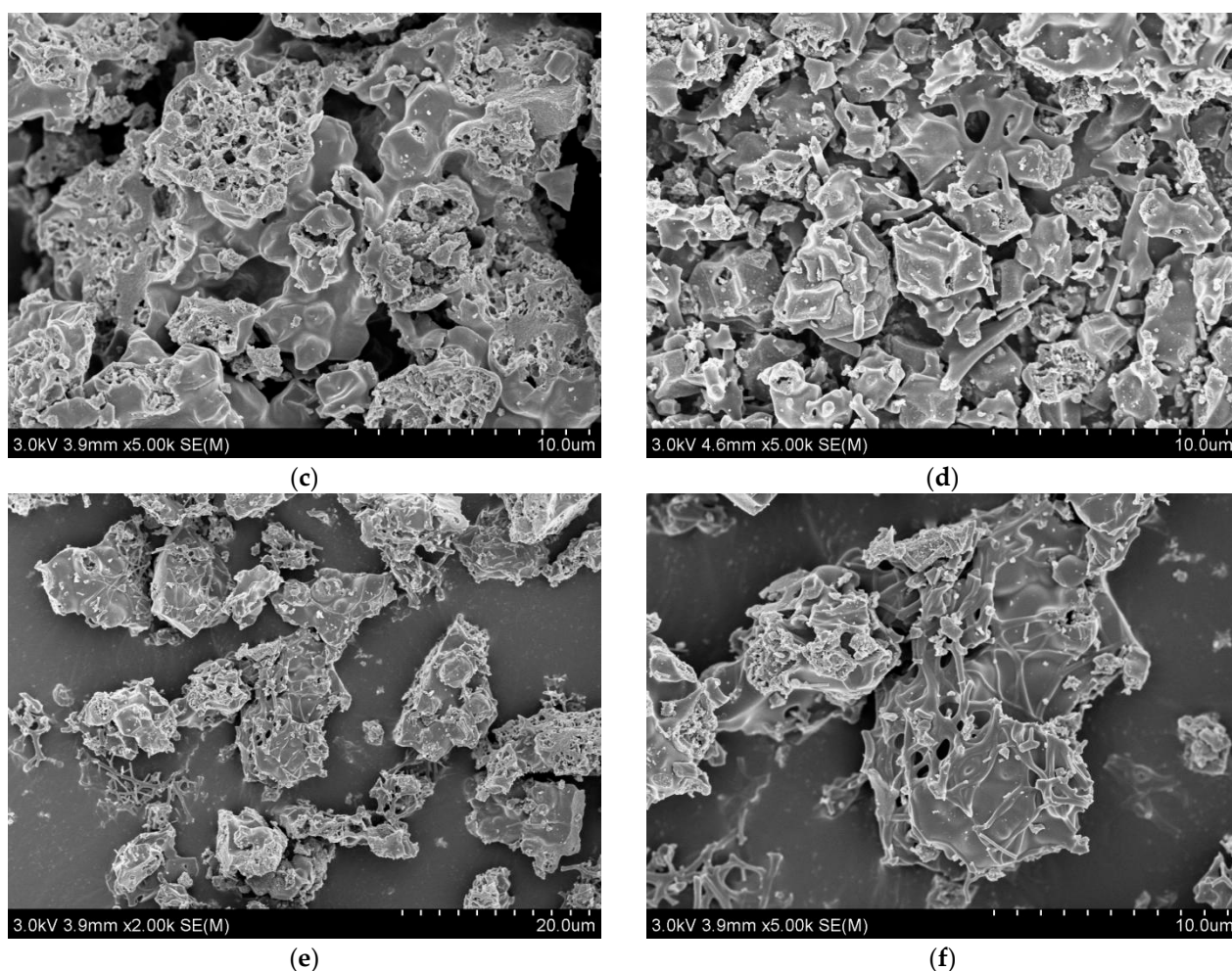


Figure 1. SEM images of (a) ZIF-67, (b) Z600, (c) ZP400, (d) ZP800 and (e, f) ZP600.

FTIR was applied to analyze the surface functional groups of the synthesized products. The pattern of ZIF-67 was consistent with the previous report [28]. The peaks of $600\text{--}1500\text{ cm}^{-1}$ in the spectrum (Figure 2) of ZIF-67 were caused by the stretching and bending modes of the imidazole ring. The peak at 1448 cm^{-1} was generated from the stretching of C=N bond in 2-MeIM. The peaks at 2929 and 3135 cm^{-1} were attributed to C-H bonds [29]. Moreover, it was noticed that ZP400 showed a similar pattern to ZIF-67, and there was no obvious characteristic peak of 2-MeIM in the patterns of ZP600 and ZP800. This result indicated that the structure of ZIF-67 may not have been completely destroyed when the calcination temperature was $400\text{ }^{\circ}\text{C}$, which was further confirmed by the subsequent XRD analysis. Furthermore, peaks at 664 and 578 cm^{-1} in the pattern of ZP800 were caused by the Co-O bond [30].

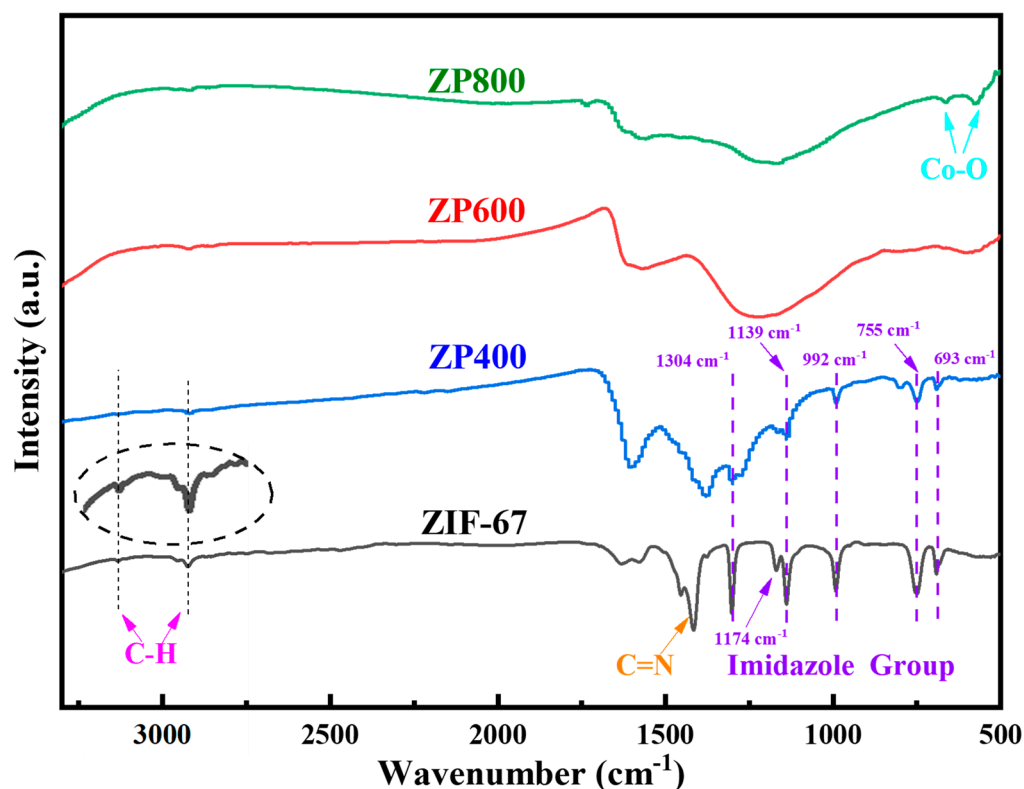


Figure 2. FTIR patterns of ZIF-67, ZP400, ZP600 and ZP800.

XRD was applied to further investigate the crystallographic structures of synthesized products. From the XRD pattern (Figure 3a) of ZIF-67, it can be seen that the peaks of the synthesized ZIF-67 perfectly matched with the previous report, which further proved the successful synthesis of ZIF-67 crystals [31]. The characteristic peaks of ZP400 were in accordance with ZIF-67, which indicated that the crystal structure of ZIF-67 was well maintained during calcination at 400 °C. From the XRD patterns (Figure 3b) of ZP600, ZP800 and Z600, it could be seen that all of them showed the characteristic peaks of the cobalt phase (JCPDS No. 15-0806), and pattern diffraction peaks at 44.2°, 51.5° and 75.8° corresponded to the (1, 1, 1), (2, 0, 0) and (2, 2, 0) crystal facets of the cobalt phase, respectively [32]. Furthermore, the peak at 26.5° was attributed to graphitic carbon in ZP600 and ZP800 [33], and that peak was missing in the pattern of Z600, which indicated that the peak of graphitic carbon was mainly caused by the carbonized PAN fibers rather than carbonized ZIF-67. In addition, it was noticed that when the carbonization temperature increased from 600 °C to 800 °C, the characteristic peaks of both cobalt phase and graphitic carbon were enhanced, indicating that the crystallization degrees were improved. That trend was consistent with the previous report [34]. In addition, peaks at 36.5° and 42.4° in the pattern of ZP800 could be assigned to (1, 1, 1) and (2, 0, 0) planes of CoO crystal lattice, which was consistent with the FTIR results [35], while the peak at 47.4° in Z600 was caused by the (1, 0, 1) crystal facet of hexagonal close packed (HCP) cobalt [36]. Compared with Z600, the intensities of cobalt peaks in ZP600 were much weaker. This result also suggested that ZP600 may have less cobalt leaching due to the cover of the cage-like PAN fibers, which was confirmed later in this work.

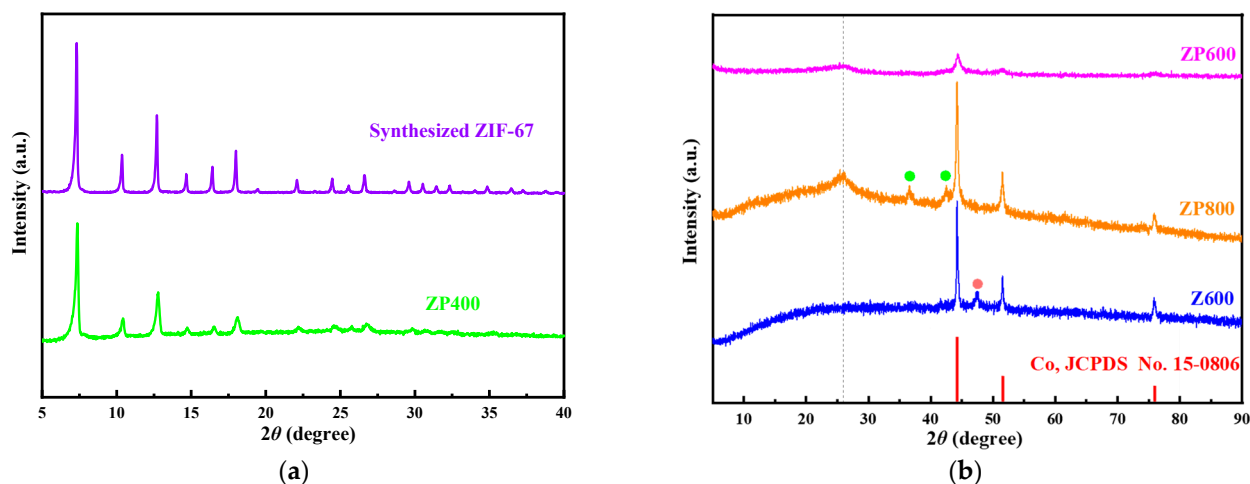


Figure 3. XRD patterns of (a) ZIF-67, ZP400, (b) ZP600, ZP800 and Z600.

TEM and energy dispersive spectroscopy (EDS) were carried out to further characterize the internal structure and element distribution of ZP600. From the TEM images (Figure 4a) of ZP600, it can be seen that the cage-like PAN fiber structure spread uniformly all over the composite, which further indicated the effect of binding cobalt leaching. The element mapping results (Figure 4b–f) showed that C, N, O and Co were distributed uniformly in ZP600, and the EDS result showed that the atomic ratio of C:N:O:Co in ZP600 was 88.37:3.40:2.90:5.34.

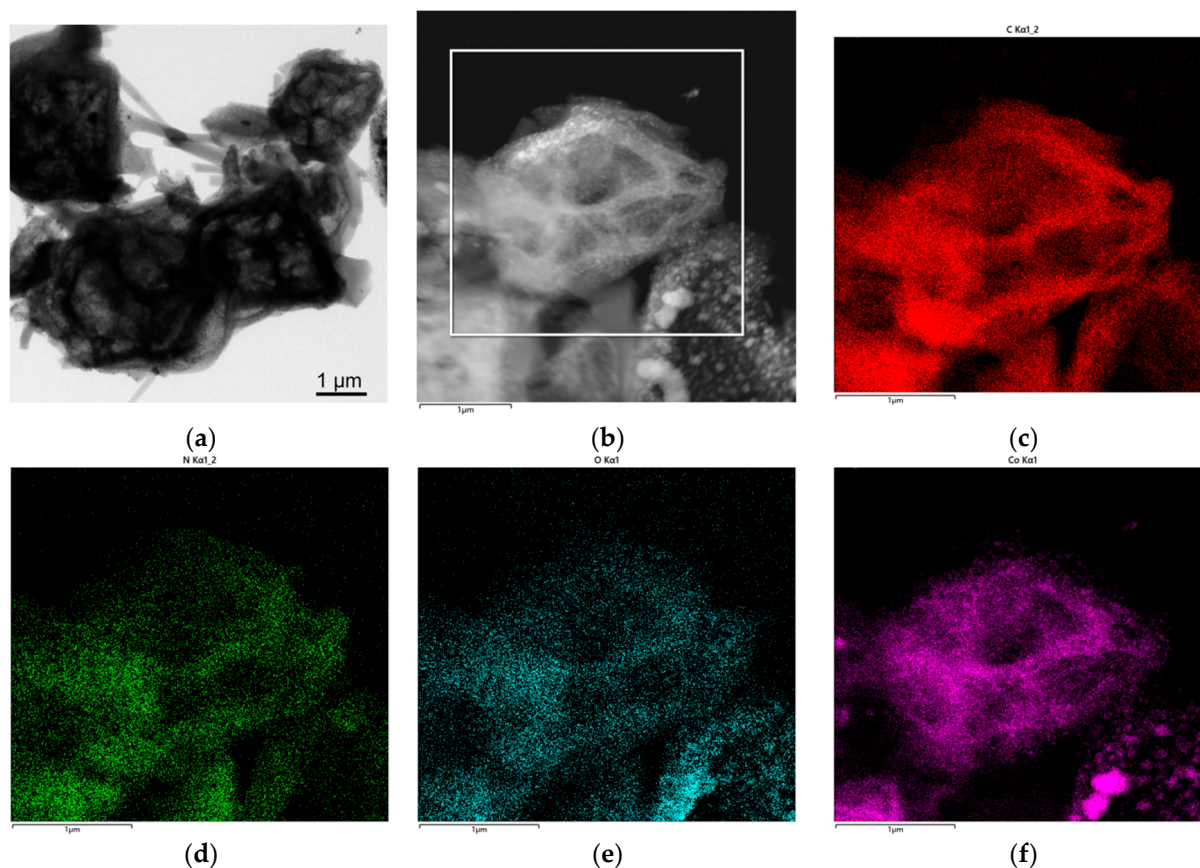


Figure 4. (a) TEM image of ZP600; (b–f) elemental mapping revealing the elemental distribution of C, N, O and Co in ZP600.

XPS was applied to analyze the surface elements composition of the synthesized ZP600. From the image of the wide-range XPS spectrum (Figure 5a), we noticed that there were four main peaks. They were C 1s, N 1s, O 1s and Co 2p, with the relative contents of 79.6%, 12.2%, 6.6% and 1.6%, respectively. It was reported that the relative contents of C, N, O and Co in ZIF-67 derived Co-N-C material (ZIF-67 powder calcined in nitrogen atmosphere at 600 °C) were 83.01%, 6.46%, 7.46% and 3.07% respectively [37]. Obviously, the content of nitrogen in the catalyst was significantly improved after applying the electrospinning process, and it was also rich in carbon, which was consistent with our assumption. It can also be seen from the N 1s XPS spectrum (Figure 5b) that peaks located at 398.37, 399.07, 400.17 and 404.48 eV corresponded to pyridinic N (37.5%), pyrrolic N (3.3%), graphitic N (49.4%) and oxidized N (9.8%), respectively [38]. Besides, it has been reported that Co 2p peaks may be weakened due to the cover layer on the surface of ZIF-67 derived cobalt-containing carbon [39]. In this work, the PAN fiber may play the same role as a cover layer that weakens the Co 2p peak. Thus, it can be speculated that the actual content of cobalt might be slightly higher. The Co 2p spectrum (Figure 5c) was analyzed to determine the existing forms and relative contents of cobalt on the surface of ZP600. Peaks at 778.3/793.3 eV (19.4%), 781.9/797.6 eV (43.1%) and 780.1/795.5 eV (37.5%) corresponded to Co⁰, Co(II) and Co(III), respectively [40,41]. The spectrum indicated that Co(II) and Co(III) were the main forms of cobalt on the surface of ZP600. As shown in the Co 2p spectrum of ZP800 (Figure 5d), the contents of Co⁰, Co²⁺ and Co³⁺ on the surface of ZP800 were 7.8%, 37.3% and 54.9%, respectively. It was noticed that when the calcination temperature increased from 600 °C to 800 °C, the content of Co⁰ decreased and the content of Co³⁺ increased. This could be evidence that ZP800 had a higher oxidation degree than ZP600, which was consistent with the above characterization results.

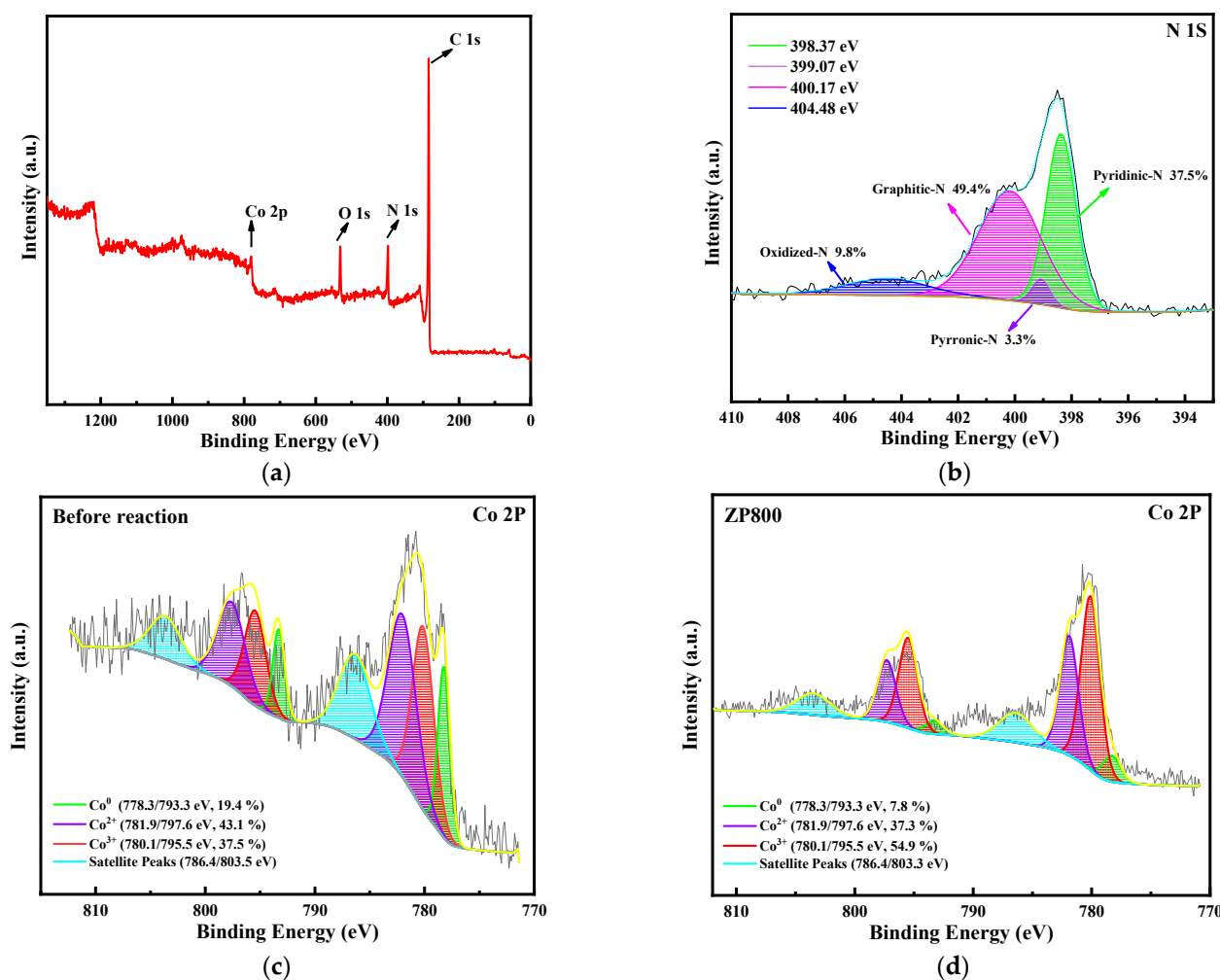


Figure 5. The wide-range XPS spectrum (a), N 1s spectrum (b) and Co 2p spectrum (c) of ZP600; (d) Co 2p spectrum of ZP800.

3.2. Degradation of DMP

3.2.1. Performance of ZP400/600/800 and Z600

ZP400, ZP600 and ZP800 were made originally from ZIF-67&PAN nanofibers carbonized at different temperatures. Their catalytic properties were investigated by batch experiments of activating PMS to degrade DMP. In terms of adsorption capacity (Figure 6), 1.1%, 8.5% and 30.3% of DMP were removed by ZP400, ZP600 and ZP800 in 30 min, respectively. Results showed that the adsorption capacities of the materials were greatly improved with the increase of carbonizing temperature in this work. A similar tendency was reported in nitrogen-doped mesoporous carbon materials by Li [42], and it has been reported that the specific surface area of ZIF-67 derived carbon materials increased when the calcination temperatures were 550 °C, 600 °C and 800 °C (159.95, 398.14 and 422.44 m²/g to 550 °C, 600 °C and 800 °C, respectively), which was similar to this work [34]. The improvement of the specific surface area of materials led to the improvement of adsorption capacity. After adding PMS, the total degradation efficiencies of DMP in 60 min were 69.2%, 85.9% and 32.4% for ZP400, ZP600 and ZP800 respectively. The DMP was hardly degraded in the group without any catalyst. For ZP800, the small difference between adsorption efficiency (30.3%) and total degradation efficiency (32.4%) implied low catalytic ability, which could be ascribed to the complete decomposition of the ZIF-67 structure above 700 °C [34]. Among all catalysts, ZP600 had the best catalytic degradation performance. Therefore, 600 °C was selected as the optimal carbonizing temperature for subsequent research. Besides, the pristine ZIF-67 powder treated by the same calcination procedure at 600 °C was named Z600. Comparing with ZP600, Z600 showed a poor adsorption capacity. Only 3% of DMP was removed by adsorption of Z600. As for catalytic performance, Z600 showed a good removal rate in the first 10 min, but the degradation efficiency remained stable with a maximum removal of 75% in the end. Therefore, the loading of PAN fibers before the calcination process did play an important role in improving the catalytic activity in this work.

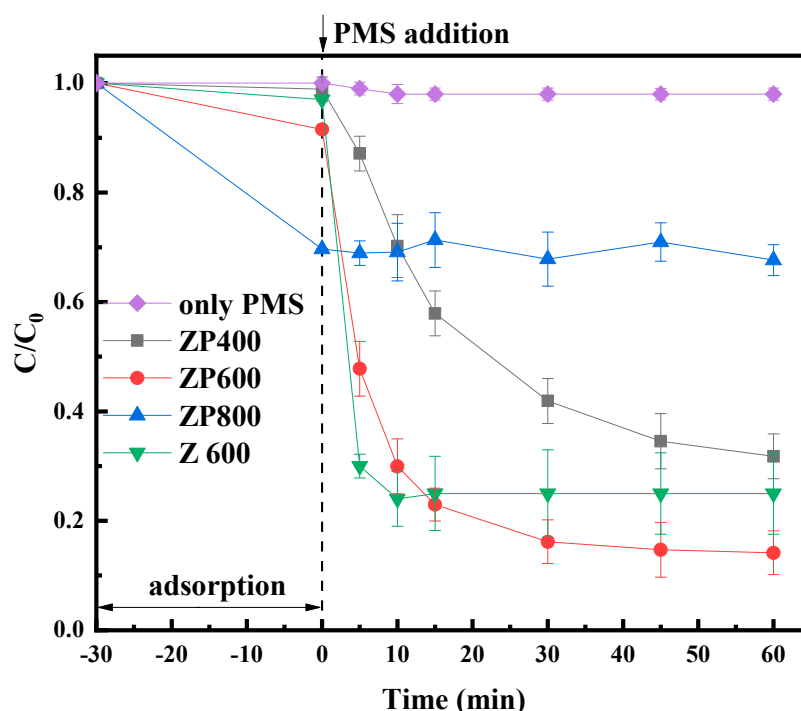


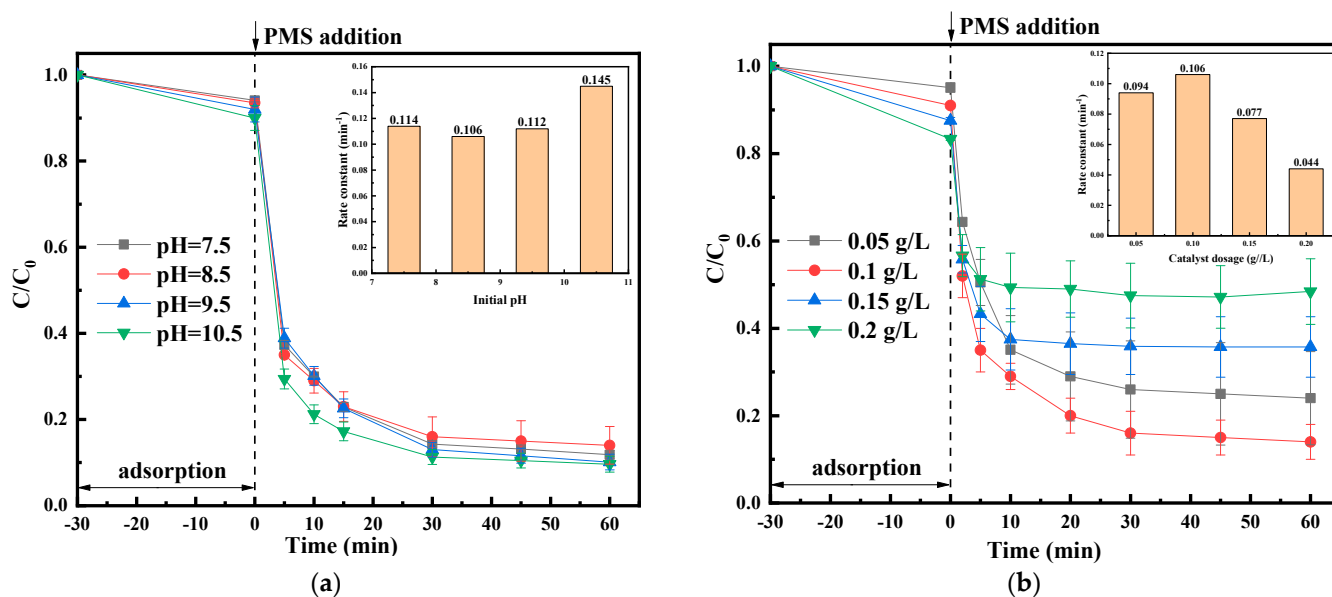
Figure 6. DMP degradation efficiency in different reaction systems within 60 min. Reaction conditions: initial pH = 8.5, catalyst = 0.1 g/L, PMS = 0.5 mM, and DMP = 6 ppm.

3.2.2. Effect of Initial pH

Several factors affecting the catalytic degradation of DMP by PMS/ZP600 were studied. As can be seen from Figure 7a, the initial pH slightly affected the adsorption capacity of ZP600. With the increase of initial pH, the adsorption capacity also gradually increased. When the initial pH values were 7.5, 8.5, 9.5 and 10.5, the adsorption rates of DMP were 5.0%, 6.5%, 8.0% and 10%, respectively. This may be due to the fact that the electrical properties of DMP molecules were changing with the adjustment of the initial pH [43]. When the pH of the solution was less than 8.59, DMPs were electrically neutral molecules [44]. When the pH₀ was higher than 8.59, DMPs changed to negatively charged molecules. It could be predicted that when the solution pH increased gradually, negatively charged DMP molecules were more likely to form electrostatic attraction with catalysts containing metal ions on the surface, thus increasing the adsorption capacity of ZP600. Meanwhile, the initial pH had little effect on the final efficiency of DMP degradation. When initial pH values were set at 7.5, 8.5, 9.5 and 10.5, the final removal efficiencies of DMP were 88.2%, 86%, 89.9% and 90.4%, respectively. This implied that ZP600 could be potentially applied in a wide range of pH₀. A similar phenomenon was reported by Zhang et al., and the ZIF-67 derived Co₃O₄/C@SiO₂ yolk-shell nanoreactors showed good adaptability to initial pH varying from 7 to 10 in the catalytic degradation of bisphenol A [39]. Moreover, the kinetics of the reaction were also studied. It was reported that the degradation of DMP by PMS accorded with the first-order reaction kinetic model [45,46]. The reaction kinetic constant k was calculated according to equation (1).

$$\ln \frac{C_t}{C_0} = -kt \quad (1)$$

Where C_t and C_0 (mg/L) were the sampling time and initial concentration of DMP, k (min⁻¹) was the rate constant, and t (min) stood for time. In this part, when the initial pH values were 7.5, 8.5, 9.5 and 10.5, the rate constants were 0.114, 0.106, 0.112 and 0.145 min⁻¹, respectively. It was noticed that the rate constants changed slightly with a different initial pH, which was consistent with changes in removal efficiency.



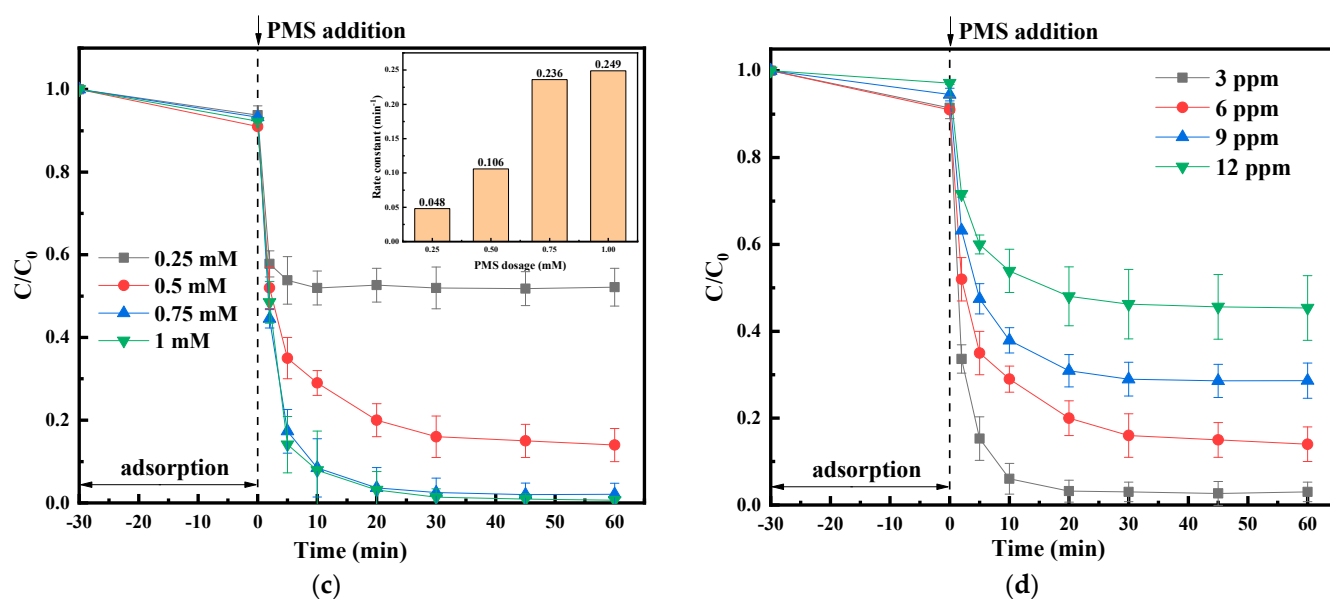
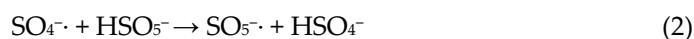


Figure 7. Effects of different initial pH (a), catalyst dosage (b), PMS dosage (c) and DMP concentration (d) on the DMP removal efficiency. Reaction conditions: initial solution pH = 8.5 (for b–d); catalyst = 0.1 g/L (for a,c,d); PMS = 0.5 mM (for a,b,d); DMP = 6 ppm (for a–c).

3.2.3. Effect of Catalyst Dosage

Obviously, with the increase of catalyst dosage, the adsorption rate of the contaminant also increased proportionally (Figure 7b). When the catalyst dosages were 0.05, 0.10, 0.15 and 0.20 g/L, the adsorption rates of DMP were 4.9%, 9.0%, 12.5% and 16.7%, respectively. In Xu's work, a similar trend was reported that the adsorption of DMP increased with the increase of the dosage of graphene-based CoFe₂O₄ [2]. This could be attributed to the fact that adsorption sites increased with the increase of catalyst dosage, resulting in an increase in adsorption capacity. In the degradation section, the removal efficiencies were 76%, 86%, 64.3% and 51.6% when the dosages were 0.05, 0.10, 0.15 and 0.20 g/L, respectively. And the degradation rate constants were also calculated, turning out to be 0.094, 0.106, 0.077 and 0.044 min⁻¹, respectively, in the order of the increase of the input of catalysts. It was noticed that both the rate constant and removal efficiency of DMP were limited when the catalyst dosage was low (0.05 g/L). This problem could be simply solved by increasing the dosage to 0.10 g/L, thereby increase the number of catalytic active sites. However, when the dosage increased to 0.15 and 0.20 g/L, both the rate constant and removal efficiency began to drop. This phenomenon was reported as diffusion limitation, which occurred when the catalyst dose was further beyond the optimal value [47].



Specifically, when a large amount of sulfate radicals was generated in a short time, side reactions would occur, such as the reaction between SO₄^{·-} and HSO₅⁻, resulting in the formation of SO₅^{·-}, which had a lower oxidizability (Equation (2)). Furthermore, the self-quenching reaction of SO₄^{·-} would also occur (Equation (3)), which led to a waste of ROS. According to Zhang's report, in the PMS/CuFe₂O₄ system, when the dosage of catalyst exceeded the optimal value (0.5 g/L), both the reaction rate constant and the removal efficiency of the pollutant (iopromide) decreased obviously [48]. Therefore, the degradation efficiency was not always positively related to the input of catalyst, and the optimal dosage varied with materials.

3.2.4. Effect of PMS Dosage

The effects of PMS dosage were also studied to determine the optimum reaction condition. It was noticed (Figure 7c) that when the PMS dosage was 0.25 mM, only 48% of DMP could be removed after the reaction. This may be due to the fact that the amount of oxidant was not sufficient to remove more contaminants. When the PMS input increased to 0.5 mM, the removal efficiency of DMP improved to 86%. Furthermore, 98% of DMP could be removed in 30 min when the PMS dosage increased to 0.75 mM. Therefore, further increasing the dosage of PMS had no significant effect on the removal of contaminant. Furthermore, the removal efficiency of 1 mM PMS input was 99.3%. A similar trend was also observed in the rate constant results. The k value increased rapidly from 0.048 to 0.106 and 0.236 min^{-1} , when the PMS dosage increased from 0.25 to 0.5 and 0.75 mM. Likewise, it showed little growth (0.236 to 0.249 min^{-1}) when the dosage increased from 0.75 to 1 mM. This phenomenon was consistent with most reports in this field. Dai et al. developed a novel ZIF-8/ZIF-67 derived Co/N co-doped carbonaceous polyhedron for PMS activation [49]. In that work, when the dosage of PMS reached 0.2 g/L, the removal efficiency of contaminant (Orange II) would no longer increase, and the growth of the degradation rate constant also slowed down. A similar result was obtained for the catalytic degradation of Rhodamine B by a NiO-NiFe₂O₄-rGO magnetic nanomaterial, which showed that the removal rate remained almost unchanged when the PMS dosage increased from 1.0 to 2.5 g/L [50]. Therefore, in the practical application of SR-AOPs, the optimal dosage of reagents is worth investigating.

3.2.5. Effect of DMP Concentration

The degradation of DMP with different concentrations was studied by batch experiments. As can be seen from Figure 7d, for different initial DMP concentrations, the adsorption rates were all within 10%, but the removal efficiencies of catalytic section showed obvious differences. When the initial concentrations of DMP were 3, 6, 9 and 12 ppm, the removal efficiencies were 97%, 84%, 71% and 55%, respectively. With the increase of the initial concentration of DMP, its removal efficiency decreased gradually. When the initial concentration was 3 ppm, 94% of DMP could be removed in 20 min. However, when it increased to 12 ppm, the removal efficiency of the whole reaction was only 55%. This phenomenon was attributed to the fact that the amount of PMS added was not enough for the degradation of contaminant when the concentration of pollutant was high [51]. This result was in agreement with Xu's report of a graphene-based CoFe₂O₄/PMS system in the catalytic degradation of DMP [2]. In that work, when the concentration of DMP increased from 12 to 20 ppm, the removal efficiency decreased by about 10%. Moreover, in this work, when the concentrations were 3, 6, 9 and 12 ppm, the net removal amounts of DMP were 2.9, 5.0, 6.4 and 6.6 ppm, respectively. This implied that the utilization efficiency of ROS increased with the increase of pollutant concentration [52].

3.3. Probable Mechanism and Reusability

Quenching experiments were carried out to investigate the activation mechanism in ZP600/PMS system. It was widely acknowledged that $\cdot\text{OH}$ and $\text{SO}_4^{\cdot-}$ would be generated in the activation of PMS by cobalt-based carbon materials [38,39]. As previously reported, TBA was mainly used to quench $\cdot\text{OH}$, while ethanol had a strong quenching effect on both $\cdot\text{OH}$ and $\text{SO}_4^{\cdot-}$ [39]. In addition, FFA was used as a quencher of $^1\text{O}_2$ according to previous reports [53]. When the concentrations of TBA were 1 and 5 mM (Figure 8a), DMP removal efficiencies decreased by 16% and 52%, respectively. When 1 and 5 mM ethanol were added into the system, the removal efficiencies of the contaminant decreased by 44% and 69%, respectively. And the degradation efficiencies of FFA-added groups had no significant change. Therefore, it was found that radicals ($\cdot\text{OH}$ and $\text{SO}_4^{\cdot-}$) were generated and played a leading role in the degradation of contaminant in this work.

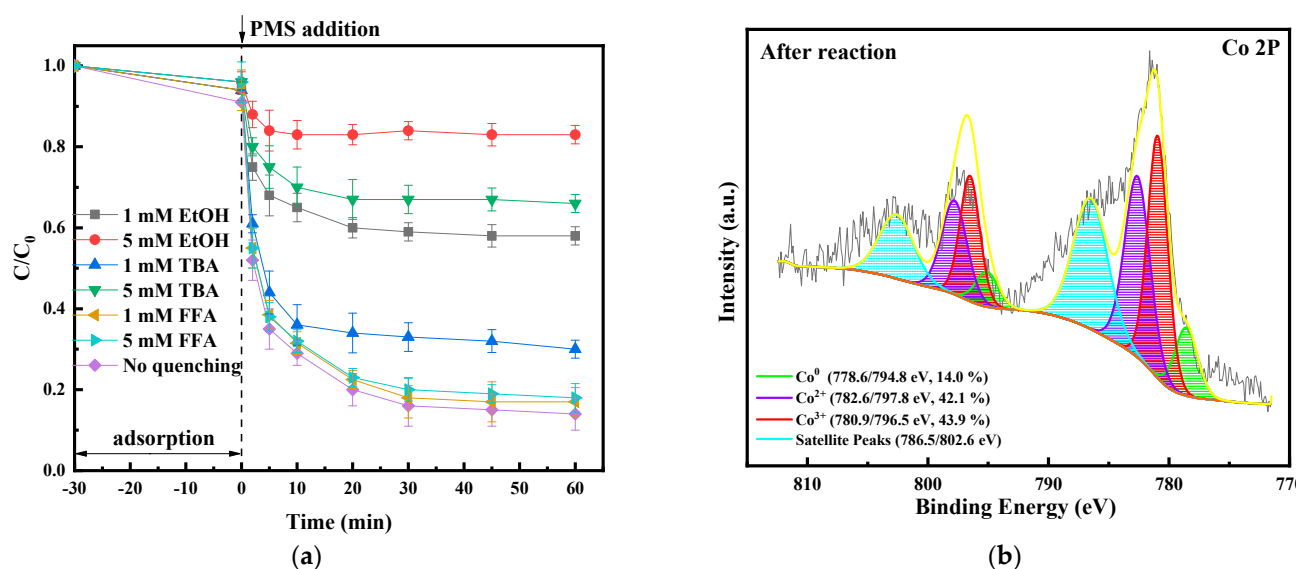
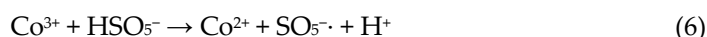
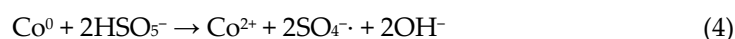


Figure 8. (a) Effects of radical scavengers on DMP degradation. (b) Co 2p XPS spectra of the ZP600 after reaction. Reaction conditions: initial solution pH = 8.5, catalyst = 0.1 g/L, PMS = 0.5 mM, and DMP = 6 ppm.

To further elaborate on the mechanism of degradation, XPS was applied to explore the changes in the valence of cobalt on the surface of ZP600 after reaction. In the image (Figure 8b) of Co 2p, peaks located at 778.6/794.8 eV (14.0%), 782.6/797.8 eV (42.1%) and 780.9/796.5 eV (43.9%) corresponded to Co⁰, Co(II) and Co(III), respectively [40,41]. This indicated that the relative content of Co⁰ on the surface of ZP600 decreased slightly after reaction, which was 19.4% before the reaction, and the ratio of Co(II)/Co(III) on the surface of ZP600 decreased slightly (from 1.15 to 0.96) after the reaction.

According to the results and previous reports [38], the probable mechanism of the cobalt-containing carbon catalyst reacting with PMS in this work might be as follows (Equations (4)–(9)):



Simply, Co⁰ and Co²⁺ of ZP600 were oxidized by HSO₅⁻ to generate SO₄^{·-} and higher valence cobalt (Co²⁺ and Co³⁺, respectively) (Equations (4) and (5)). At the same time, Co³⁺ reacted with HSO₅⁻ to create SO₅^{·-} and Co²⁺ (Equation (6)). Moreover, Co⁰ and Co³⁺ could react with each other to form Co²⁺ (Equation (7)), and the generated SO₄^{·-} can further react with OH⁻ in the solution to yield ·OH and SO₄²⁻ (Equation (8)). Finally, all the generated reactive species oxidized the template contaminant DMP to intermediates and mineralization products (Equation (9)). The TOC removal efficiency in the process was 65%, which further proved the mineralization of the contaminant (Figure 9a). In addition, it has been widely reported that the catalytic performance was positively related to the amount of doped nitrogen [54,55]. As reported, all species of nitrogen except oxidized N could promote the catalytic activity of the catalysts [56]. Due to the strong electronegativity of

graphite N, a positive charge would be induced on its adjacent carbon, thus promoting the adsorption of PMS molecules on the catalyst [57]. In addition, pyrrolic N and pyridinic N with lone-pair electrons could provide Lewis base sites to promote the adsorption of pollutants and donate electrons to PMS for radical generation [58,59].

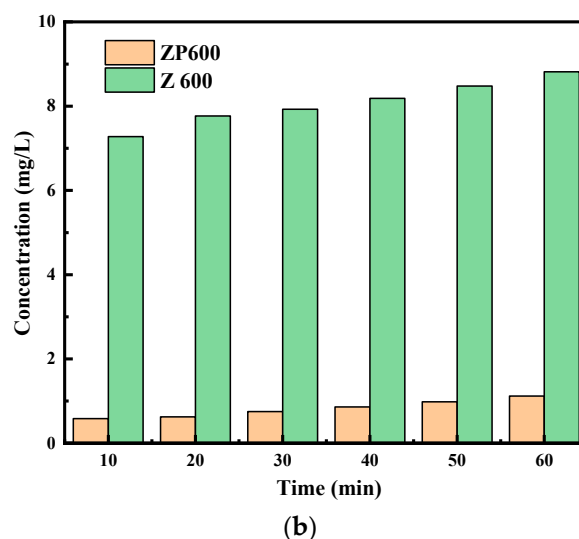
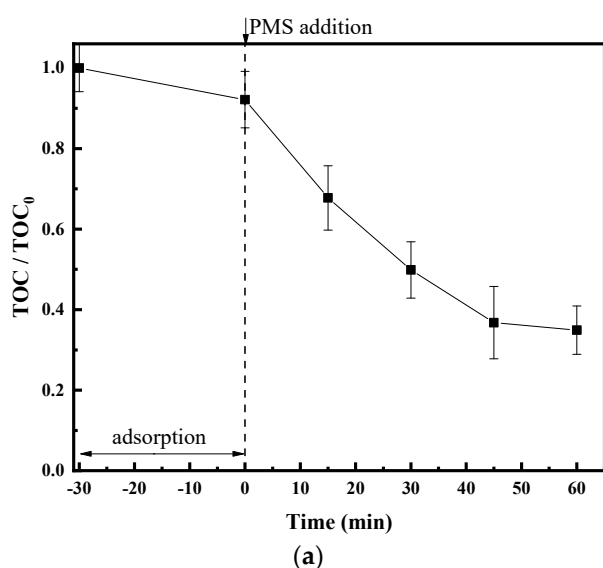
The cobalt leaching in the system of ZP600/PMS was analyzed by ICP-OES. From Figure 9b, it can be seen that the concentration of cobalt ion increased from 0.58 mg/L in the first 10 minutes to 1.12 mg/L in the end. In order to compare with Z600, cobalt leaching in the Z600/PMS system was also detected. It was found to be 7.2 mg/L in 10 min and 8.8 mg/L in the end. Results showed that ZP600 greatly reduced the cobalt leaching, and the leaching amount decreased by about 87%. In addition, cobalt loading on the catalyst and the cobalt leaching rate were also determined by aqua regia digestion and ICP test. Simply, 10 mg of a certain catalyst was digested in 25 mL of aqua regia at 170 °C for 30 min. After that, the residual liquid was diluted to a final volume of 1 L with ultrapure water for ICP test. The cobalt loadings of the catalysts were calculated according to the following equation:

$$\text{Cobalt loading (\%)} = \frac{\text{measured cobalt concentration (mg/L)} \times 1 \text{ L}}{10 \text{ mg}} \times 100\% \quad (10)$$

The cobalt leaching rate referred to the ratio of cobalt leached after the reaction to cobalt loaded on the material, which was calculated with the following equation:

$$\text{Leaching rate (\%)} = \frac{\text{cobalt leaching amount (mg/L)} \times 0.1 \text{ L}}{\text{cobalt loading (\%)} \times 10 \text{ mg}} \times 100\% \quad (11)$$

In Equation (11), 0.1 L referred to the volume of the reaction system, and 10 mg was the dosage of catalyst in the reaction. The cobalt loadings of ZP600 and Z600 were 15.1% and 40.2%, respectively. Through the combined calculation of cobalt leaching amounts and cobalt loadings, it was noticed that about 21.9% of cobalt in Z600 was leached in 60 min, while only 7.4% of cobalt in ZP600 was leached, which further proved that ZP600 had the potential to reduce cobalt leaching. It has been reported that the cobalt leaching of cobalt-containing catalysts would sharply reduce when the surface of the catalyst was covered by a covering layer [39]. In this work, the reduction of leaching was due to the cage-like cover of PAN fibers on the ZIF-67.



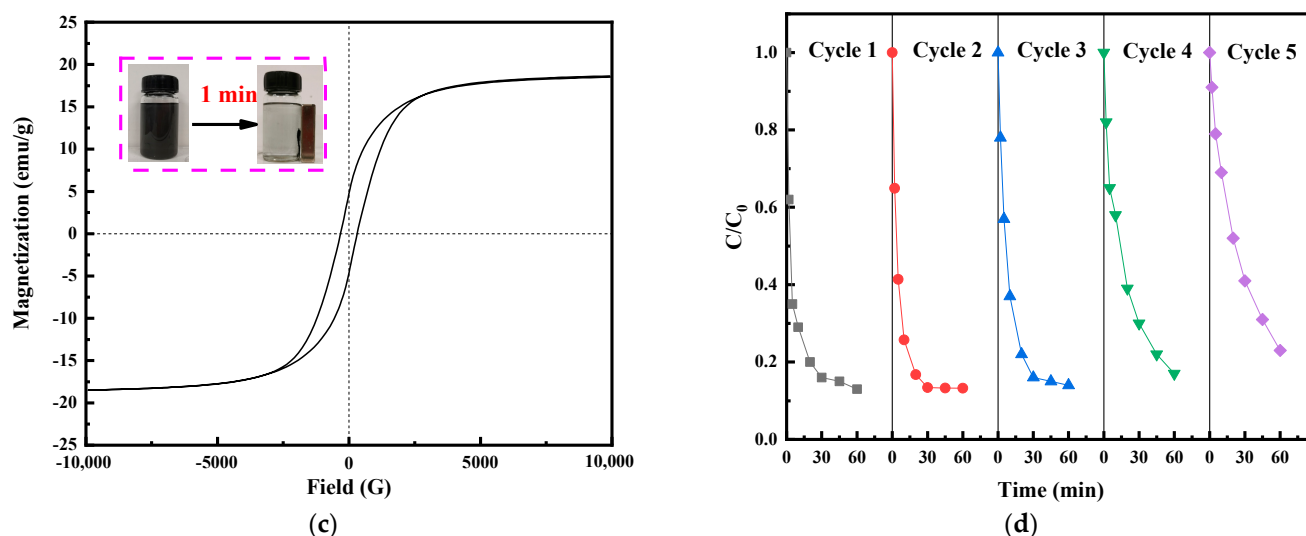


Figure 9. (a) Removal efficiency of TOC in the ZP600/PMS/DMP system; (b) Leaching of cobalt ions in the degradation process; (c) Magnetic hysteresis loops of ZP600; (d) Removal efficiency of DMP in multiple uses of ZP600. Reaction conditions: initial solution pH = 8.5, catalyst = 0.1 g/L, PMS = 0.5 mM, and DMP = 6 ppm.

Five rounds of batch experiments were carried out to evaluate the reusability of ZP600. The catalysts could be magnetically separated (insert in Figure 9c) and reused in the next round experiment without further treatment. The hysteresis loop of ZP600 was in Figure 9c. As shown in the image (Figure 9d), the catalytic performance of ZP600 was quite stable in the first three experiments, with degradation efficiencies of 87%, 87% and 86%, respectively. However, the removal efficiencies of the fourth and fifth cycles were 83% and 77%, respectively, which decreased slightly. In addition, the cobalt leaching amount after each cycle were 1.12, 0.82, 0.48, 0.16 and 0.09 mg/L, respectively. The decrease of catalytic performance might be ascribed to the loss of catalysts during reaction, recycling and sampling processes [48]. Moreover, the change of the Co(II)/Co(III) ratio in the catalyst detected by XPS may also lead to a loss of catalytic activity gradually.

4. Conclusions

In summary, we applied electrospinning as a technique to synthesize a cobalt-based PMS activator that was rich in carbon and nitrogen. The synthesized ZP600 showed great performance (90.4% removal rate was achieved in 60 min) in degrading DMP under a wide range of pH in a radical-dominated mechanism. Due to the good magnetism, ZP600 could be easily separated from water and showed great stability in five-cycle experiments. Radicals were identified as the main ROS to degrade pollutants. To our surprise, it was found that PAN nanofibers could largely reduce cobalt leaching by about 87% from the catalyst. This work would not only extend the application of the electrospinning technique for water purification but also give inspiration for researches aiming to control the leaching of harmful substances.

Author Contributions: Conceptualization, Y.Z.; methodology, G.P., Z.L., Z.Y., X.Q.; software, G.P.; validation, M.J. and Y.Z.; formal analysis, G.P.; data curation, G.P.; writing—original draft preparation, G.P.; writing—review and editing, Y.Z., M.J.; supervision, M.J.; funding acquisition, M.J. All authors have read and agreed to the published version of the manuscript.

Funding: This research was funded by the Tianjin Science and Technology Plan Project (No. 19ZXSZSN00080) and the Young Elite Scientists Sponsorship Program by Tianjin (TJSQNTJ-2020-16).

Data Availability Statement: The datasets generated during and/or analyzed during the current study are available from the corresponding author on reasonable request.

Conflicts of Interest: The authors declare no conflict of interest.

References

1. Huang, Z.; Gu, Z.; Wang, Y.; Zhang, A. Improved oxidation of refractory organics in concentrated leachate by a Fe²⁺-enhanced O₃/H₂O₂ process. *Environ. Sci. Pollut. Res.* **2019**, *26*, 35797–35806. <https://doi.org/10.1007/s11356-019-06592-y>.
2. Xu, L.J.; Chu, W.; Gan, L. Environmental application of graphene-based CoFe₂O₄ as an activator of peroxymonosulfate for the degradation of a plasticizer. *Chem. Eng. J.* **2015**, *263*, 435–443. <https://doi.org/10.1016/j.cej.2014.11.065>.
3. Karim, A.V.; Krishnan, S.; Sethulekshmi, S. *New Trends in Emerging Environmental Contaminants. Energy, Environment, and Sustainability*, 3rd ed.; Springer: Singapore, 2022; pp. 131–160. https://doi.org/10.1007/978-981-16-8367-1_7.
4. Shi, J.; Han, Y.; Xu, C.; Han, H. Biological coupling process for treatment of toxic and refractory compounds in coal gasification wastewater. *Rev. Environ. Sci. Bio/Technol.* **2018**, *17*, 765–790. <https://doi.org/10.1007/s11157-018-9481-2>.
5. Bilińska, L.; Gmurek, M.; Ledakowicz, S. Textile wastewater treatment by AOPs for brine reuse. *Process Saf. Environ. Prot.* **2017**, *109*, 420–428. <https://doi.org/10.1016/j.psep.2017.04.019>.
6. Yang, Q.; Choi, H.; Al-Abed, S.R.; Dionysiou, D.D. Iron–cobalt mixed oxide nanocatalysts: Heterogeneous peroxymonosulfate activation, cobalt leaching, and ferromagnetic properties for environmental applications. *Appl. Catal. B Environ.* **2009**, *88*, 462–469. <https://doi.org/10.1016/j.apcatb.2008.10.013>.
7. Oh, W.; Dong, Z.; Lim, T. Generation of sulfate radical through heterogeneous catalysis for organic contaminants removal: Current development, challenges and prospects. *Appl. Catal. B Environ.* **2016**, *194*, 169–201. <https://doi.org/10.1016/j.apcatb.2016.04.003>.
8. He, Y.; Zhang, J.; Zhou, H.; Yao, G.; Lai, B. Synergistic multiple active species for the degradation of sulfamethoxazole by peroxymonosulfate in the presence of CuO@FeO_x@Fe⁰. *Chem. Eng. J.* **2020**, *380*, 122568. <https://doi.org/10.1016/j.cej.2019.122568>.
9. Kohantorabi, M.; Moussavi, G.; Giannakis, S. A review of the innovations in metal- and carbon-based catalysts explored for heterogeneous peroxymonosulfate (PMS) activation, with focus on radical vs. non-radical degradation pathways of organic contaminants. *Chem. Eng. J.* **2021**, *411*, 127957. <https://doi.org/10.1016/j.cej.2020.127957>.
10. Wang, J.; Wang, S. Activation of persulfate (PS) and peroxymonosulfate (PMS) and application for the degradation of emerging contaminants. *Chem. Eng. J.* **2018**, *334*, 1502–1517. <https://doi.org/10.1016/j.cej.2017.11.059>.
11. Ghanbari, F.; Moradi, M. Application of peroxymonosulfate and its activation methods for degradation of environmental organic pollutants: Review. *Chem. Eng. J.* **2017**, *310*, 41–62. <https://doi.org/10.1016/j.cej.2016.10.064>.
12. Yao, Y.; Cai, Y.; Wu, G.; Wei, F.; Li, X.; Chen, H.; Wang, S. Sulfate radicals induced from peroxymonosulfate by cobalt manganese oxides (Co_xMn_{3-x}O₄) for Fenton-Like reaction in water. *J. Hazard. Mater.* **2015**, *296*, 128–137. <https://doi.org/10.1016/j.jhazmat.2015.04.014>.
13. Li, W.; Wu, P.; Yang, S.; Zhu, Y.; Kang, C.; Tran, L.T.; Zeng, B. 3D hierarchical honeycomb structured MWCNTs coupled with CoMnAl-LDO: Fabrication and application for ultrafast catalytic degradation of bisphenol A. *RSC Adv.* **2015**, *5*, 8859–8867. <https://doi.org/10.1039/C4RA15339A>.
14. Deng, J.; Shao, Y.; Gao, N.; Tan, C.; Zhou, S.; Hu, X. CoFe₂O₄ magnetic nanoparticles as a highly active heterogeneous catalyst of oxone for the degradation of diclofenac in water. *J. Hazard. Mater.* **2013**, *262*, 836–844. <https://doi.org/10.1016/j.jhazmat.2013.09.049>.
15. Anipsitakis, G.P.; Stathatos, E.; Dionysiou, D.D. Heterogeneous Activation of Oxone Using Co₃O₄. *J. Phys. Chem. B* **2005**, *109*, 13052–13055. <https://doi.org/10.1021/jp052166y>.
16. Chen, X.; Chen, J.; Qiao, X.; Wang, D.; Cai, X. Performance of nano-Co₃O₄/peroxymonosulfate system: Kinetics and mechanism study using Acid Orange 7 as a model compound. *Appl. Catal. B Environ.* **2008**, *80*, 116–121. <https://doi.org/10.1016/j.apcatb.2007.11.009>.
17. Lin, K.A.; Chang, H. Zeolitic Imidazole Framework-67 (ZIF-67) as a heterogeneous catalyst to activate peroxymonosulfate for degradation of Rhodamine B in water. *J. Taiwan Inst. Chem. Eng.* **2015**, *53*, 40–45. <https://doi.org/10.1016/j.jtice.2015.02.027>.
18. Dong, Y.Z.; Piao, S.H.; Zhang, K.; Choi, H.J. Effect of CoFe₂O₄ nanoparticles on a carbonyl iron based magnetorheological suspension. *Colloids Surf. A Physicochem. Eng. Asp.* **2018**, *537*, 102–108. <https://doi.org/10.1016/j.colsurfa.2017.10.017>.
19. Xiong, Z.; Jiang, Y.; Wu, Z.; Yao, G.; Lai, B. Synthesis strategies and emerging mechanisms of metal-organic frameworks for sulfate radical-based advanced oxidation process: A review. *Chem. Eng. J.* **2021**, *421*, 127863. <https://doi.org/10.1016/j.cej.2020.127863>.
20. Duan, X.; Sun, H.; Wang, Y.; Kang, J.; Wang, S. N-Doping-Induced Nonradical Reaction on Single-Walled Carbon Nanotubes for Catalytic Phenol Oxidation. *ACS Catal.* **2015**, *5*, 553–559. <https://doi.org/10.1021/cs5017613>.
21. Xue, Y.; Pham, N.N.T.; Nam, G.; Choi, J.; Ahn, Y.; Lee, H.; Jung, J.; Lee, S.; Lee, J. Persulfate activation by ZIF-67-derived cobalt/nitrogen-doped carbon composites: Kinetics and mechanisms dependent on persulfate precursor. *Chem. Eng. J.* **2021**, *408*, 127305. <https://doi.org/10.1016/j.cej.2020.127305>.
22. Bao, Y.; Tian, M.; Lua, S.K.; Lim, T.; Wang, R.; Hu, X. Spatial confinement of cobalt crystals in carbon nanofibers with oxygen vacancies as a high-efficiency catalyst for organics degradation. *Chemosphere* **2020**, *245*, 125407. <https://doi.org/10.1016/j.chemosphere.2019.125407>.

23. Wang, C.; Wang, H.; Luo, R.; Liu, C.; Li, J.; Sun, X.; Shen, J.; Han, W.; Wang, L. Metal-organic framework one-dimensional fibers as efficient catalysts for activating peroxydisulfate. *Chem. Eng. J.* **2017**, *330*, 262–271. <https://doi.org/10.1016/j.cej.2017.07.156>.
24. Wang, Z.; Yang, N.; Wang, D. When hollow multishelled structures (HoMSs) meet metal-organic frameworks (MOFs). *Chem. Sci.* **2020**, *11*, 5359–5368. <https://doi.org/10.1039/d0sc01284j>.
25. Ventura, K.; Arrieta, R.A.; Marcos-Hernández, M.; Jabbari, V.; Powell, C.D.; Turley, R.; Lounsbury, A.W.; Zimmerman, J.B.; Gardea-Torresdey, J.; Wong, M.S.; et al. Superparamagnetic MOF@GO Ni and Co based hybrid nanocomposites as efficient water pollutant adsorbents. *Sci. Total Environ.* **2020**, *738*, 139213. <https://doi.org/10.1016/j.scitotenv.2020.139213>.
26. Qian, J.; Sun, F.; Qin, L. Hydrothermal synthesis of zeolitic imidazolate framework-67 (ZIF-67) nanocrystals. *Mater. Lett.* **2012**, *82*, 220–223. <https://doi.org/10.1016/j.matlet.2012.05.077>.
27. Guo, J.; Chen, B.; Hao, Q.; Nie, J.; Ma, G. Pod-like structured Co/CoO_x nitrogen-doped carbon fibers as efficient oxygen reduction reaction electrocatalysts for Zn-air battery. *Appl. Surf. Sci.* **2018**, *456*, 959–966. <https://doi.org/10.1016/j.apsusc.2018.05.210>.
28. Khan, A.; Ali, M.; Ilyas, A.; Naik, P.; Vankelecom, I.F.J.; Gilani, M.A.; Bilad, M.R.; Sajjad, Z.; Khan, A.L. ZIF-67 filled PDMS mixed matrix membranes for recovery of ethanol via pervaporation. *Sep. Purif. Technol.* **2018**, *206*, 50–58. <https://doi.org/10.1016/j.seppur.2018.05.055>.
29. Qin, J.; Wang, S.; Wang, X. Visible-light reduction CO₂ with dodecahedral zeolitic imidazolate framework ZIF-67 as an efficient co-catalyst. *Appl. Catal. B Environ.* **2017**, *209*, 476–482. <https://doi.org/10.1016/j.apcatb.2017.03.018>.
30. Jonynaite, D.; Senvaitiene, J.; Beganskiene, A.; Kareiva, A. Spectroscopic analysis of blue cobalt smalt pigment. *Vib. Spectrosc.* **2010**, *52*, 158–162. <https://doi.org/10.1016/j.vibspec.2009.12.005>.
31. Zhang, X.; Yan, X.; Hu, X.; Feng, R.; Zhou, M.; Wang, L. Efficient removal of organic pollutants by a Co/N/S-doped yolk-shell carbon catalyst via peroxydisulfate activation. *J. Hazard. Mater.* **2022**, *421*, 126726. <https://doi.org/10.1016/j.jhazmat.2021.126726>.
32. Shu, J.; Niu, Q.; Wang, N.; Nie, J.; Ma, G. Alginate derived Co/N doped hierarchical porous carbon microspheres for efficient oxygen reduction reaction. *Appl. Surf. Sci.* **2019**, *485*, 520–528. <https://doi.org/10.1016/j.apsusc.2019.04.204>.
33. Wang, N.; Ma, W.; Ren, Z.; Du, Y.; Xu, P.; Han, X. Prussian blue analogues derived porous nitrogen-doped carbon microspheres as high-performance metal-free peroxydisulfate activators for non-radical-dominated degradation of organic pollutants. *J. Mater. Chem. A* **2018**, *6*, 884–895. <https://doi.org/10.1039/C7TA08472B>.
34. Ding, S.; Zhang, C.; Liu, Y.; Jiang, H.; Xing, W.; Chen, R. Pd nanoparticles supported on N-doped porous carbons derived from ZIF-67: Enhanced catalytic performance in phenol hydrogenation. *J. Ind. Eng. Chem.* **2017**, *46*, 258–265. <https://doi.org/10.1016/j.jiec.2016.10.037>.
35. Ye, Y.; Yuan, F.; Li, S. Synthesis of CoO nanoparticles by esterification reaction under solvothermal conditions. *Mater. Lett.* **2006**, *60*, 3175–3178. <https://doi.org/10.1016/j.matlet.2006.02.062>.
36. Jung, J.; Lee, J.; Choi, G.; Ramesh, S.; Moon, D.J. The characterization of micro-structure of cobalt on γ -Al₂O₃ for FTS: Effects of pretreatment on Ru-Co/ γ -Al₂O₃. *Fuel* **2015**, *149*, 118–129. <https://doi.org/10.1016/j.fuel.2014.09.001>.
37. Wu, Z.; Sun, L.; Zhou, Z.; Li, Q.; Huo, L.; Zhao, H. Efficient nonenzymatic H₂O₂ biosensor based on ZIF-67 MOF derived Co nanoparticles embedded N-doped mesoporous carbon composites. *Sens. Actuators B Chem.* **2018**, *276*, 142–149. <https://doi.org/10.1016/j.snb.2018.08.100>.
38. Luo, J.; Bo, S.; Qin, Y.; An, Q.; Xiao, Z.; Zhai, S. Transforming goat manure into surface-loaded cobalt/biochar as PMS activator for highly efficient ciprofloxacin degradation. *Chem. Eng. J.* **2020**, *395*, 125063. <https://doi.org/10.1016/j.cej.2020.125063>.
39. Zhang, M.; Wang, C.; Liu, C.; Luo, R.; Li, J.; Sun, X.; Shen, J.; Han, W.; Wang, L. Metal-organic framework derived Co₃O₄/C@SiO₂ yolk-shell nanoreactors with enhanced catalytic performance. *J. Mater. Chem. A* **2018**, *6*, 11226–11235. <https://doi.org/10.1039/C8TA03565B>.
40. Kengne, B.F.; Alayat, A.M.; Luo, G.; McDonald, A.G.; Brown, J.; Smotherman, H.; McIlroy, D.N. Preparation, surface characterization and performance of a Fischer-Tropsch catalyst of cobalt supported on silica nanosprings. *Appl. Surf. Sci.* **2015**, *359*, 508–514. <https://doi.org/10.1016/j.apsusc.2015.10.081>.
41. Jaffari, G.H.; Lin, H.; Rumaiz, A.K.; Yassitepe, E.; Ni, C.; Shah, S.I. Comparative surface studies of oxygen passivated FeCo nanoparticles and thin films. *Phys. Status Solidi A* **2013**, *210*, 306–310. <https://doi.org/10.1002/pssa.201228540>.
42. Li, H.; An, N.; Liu, G.; Li, J.; Liu, N.; Jia, M.; Zhang, W.; Yuan, X. Adsorption behaviors of methyl orange dye on nitrogen-doped mesoporous carbon materials. *J. Colloid Interface Sci.* **2016**, *466*, 343–351. <https://doi.org/10.1016/j.jcis.2015.12.048>.
43. Han, S.; Mao, D.; Wang, H.; Guo, H. An insightful analysis of dimethyl phthalate degradation by the collaborative process of DBD plasma and Graphene-WO₃ nanocomposites. *Chemosphere* **2022**, *291*, 132774. <https://doi.org/10.1016/j.chemosphere.2021.132774>.
44. Pan, Z.; Huang, B.; Zhang, C. Preparation of a sludge-based adsorbent and adsorption of dimethyl phthalate from aqueous solution. *Desalination Water Treat.* **2016**, *57*:42, 20016–20026. <https://doi.org/10.1080/19443994.2016.1145145>.
45. Wang, S.; Wang, J. Treatment of membrane filtration concentrate of coking wastewater using PMS/chloridion oxidation process. *Chem. Eng. J.* **2020**, *379*, 122361. <https://doi.org/10.1016/j.cej.2019.122361>.
46. Zhou, P.; Zhang, J.; Zhang, G.; Li, W.; Liu, Y.; Cheng, X.; Huo, X.; Liu, Y.; Zhang, Y. Degradation of dimethyl phthalate by activating peroxydisulfate using nanoscale zero valent tungsten: Mechanism and degradation pathway. *Chem. Eng. J.* **2019**, *359*, 138–148. <https://doi.org/10.1016/j.cej.2018.11.123>.

47. Xu, X.; Chen, W.; Zong, S.; Ren, X.; Liu, D. Magnetic clay as catalyst applied to organics degradation in a combined adsorption and Fenton-like process. *Chem. Eng. J.* **2019**, *373*, 140–149. <https://doi.org/10.1016/j.cej.2019.05.030>.
48. Zhang, T.; Zhu, H.; Croué, J. Production of Sulfate Radical from Peroxymonosulfate Induced by a Magnetically Separable CuFe_2O_4 Spinel in Water: Efficiency, Stability, and Mechanism. *Environ. Sci. Technol.* **2013**, *47*, 2784–2791. <https://doi.org/10.1021/es304721g>.
49. Dai, H.; Zhou, W.; Wang, W. Co/N co-doped carbonaceous polyhedron as efficient peroxymonosulfate activator for degradation of organic pollutants: Role of cobalt. *Chem. Eng. J.* **2021**, *417*, 127921. <https://doi.org/10.1016/j.cej.2020.127921>.
50. Xu, X.; Li, Y.; Zhang, G.; Yang, F.; He, P. NiO-NiFe₂O₄-rGO Magnetic Nanomaterials for Activated Peroxymonosulfate Degradation of Rhodamine B. *Water* **2019**, *11*, 384. <https://doi.org/10.3390/w11020384>.
51. Klu, P.K.; Khan, M.A.N.; Wang, C.; Qi, J.; Sun, X.; Li, J. Mechanism of peroxymonosulfate activation and the utilization efficiency using hollow (Co, Mn)₃O₄ nanoreactor as an efficient catalyst for degradation of organic pollutants. *Environ. Res.* **2022**, *207*, 112148. <https://doi.org/10.1016/j.envres.2021.112148>.
52. Yu, C.; He, J.; Lan, S.; Guo, W.; Zhu, M. Enhanced utilization efficiency of peroxymonosulfate via water vortex-driven piezo-activation for removing organic contaminants from water. *Environ. Sci. Ecotechnol.* **2022**, *10*, 100165. <https://doi.org/10.1016/j.esec.2022.100165>.
53. Cai, H.; Zou, J.; Lin, J.; Li, J.; Huang, Y.; Zhang, S.; Yuan, B.; Ma, J. Sodium hydroxide-enhanced acetaminophen elimination in heat/peroxymonosulfate system: Production of singlet oxygen and hydroxyl radical. *Chem. Eng. J.* **2022**, *429*, 132438. <https://doi.org/10.1016/j.cej.2021.132438>.
54. Yun, E.; Moon, G.; Lee, H.; Jeon, T.H.; Lee, C.; Choi, W.; Lee, J. Oxidation of organic pollutants by peroxymonosulfate activated with low-temperature-modified nanodiamonds: Understanding the reaction kinetics and mechanism. *Appl. Catal. B Environ.* **2018**, *237*, 432–441. <https://doi.org/10.1016/j.apcatb.2018.04.067>.
55. Liu, Y.; Miao, W.; Fang, X.; Tang, Y.; Wu, D.; Mao, S. MOF-derived metal-free N-doped porous carbon mediated peroxydisulfate activation via radical and non-radical pathways: Role of graphitic N and C-O. *Chem. Eng. J.* **2020**, *380*, 122584. <https://doi.org/10.1016/j.cej.2019.122584>.
56. Chen, X.; Oh, W.; Hu, Z.; Sun, Y.; Webster, R.D.; Li, S.; Lim, T. Enhancing sulfacetamide degradation by peroxymonosulfate activation with N-doped graphene produced through delicately-controlled nitrogen functionalization via tweaking thermal annealing processes. *Appl. Catal. B Environ.* **2018**, *225*, 243–257. <https://doi.org/10.1016/j.apcatb.2017.11.071>.
57. Choi, C.H.; Park, S.H.; Woo, S.I. Binary and Ternary Doping of Nitrogen, Boron, and Phosphorus into Carbon for Enhancing Electrochemical Oxygen Reduction Activity. *ACS Nano* **2012**, *6*, 7084–7091. <https://doi.org/10.1021/nn3021234>.
58. Luo, Z.; Lim, S.; Tian, Z.; Shang, J.; Lai, L.; MacDonald, B.; Fu, C.; Shen, Z.; Yu, T.; Lin, J. Pyridinic N doped graphene: Synthesis, electronic structure, and electrocatalytic property. *J. Mater. Chem.* **2011**, *21*, 8038. <https://doi.org/10.1039/c1jm10845j>.
59. Miao, J.; Geng, W.; Alvarez, P.J.J.; Long, M. 2D N-Doped Porous Carbon Derived from Polydopamine-Coated Graphitic Carbon Nitride for Efficient Nonradical Activation of Peroxymonosulfate. *Environ. Sci. Technol.* **2020**, *54*, 8473–8481. <https://doi.org/10.1021/acs.est.0c03207>.